

# Green Chemistry

Accepted Manuscript



This is an *Accepted Manuscript*, which has been through the Royal Society of Chemistry peer review process and has been accepted for publication.

*Accepted Manuscripts* are published online shortly after acceptance, before technical editing, formatting and proof reading. Using this free service, authors can make their results available to the community, in citable form, before we publish the edited article. We will replace this *Accepted Manuscript* with the edited and formatted *Advance Article* as soon as it is available.

You can find more information about *Accepted Manuscripts* in the [Information for Authors](#).

Please note that technical editing may introduce minor changes to the text and/or graphics, which may alter content. The journal's standard [Terms & Conditions](#) and the [Ethical guidelines](#) still apply. In no event shall the Royal Society of Chemistry be held responsible for any errors or omissions in this *Accepted Manuscript* or any consequences arising from the use of any information it contains.



[www.rsc.org/greenchem](http://www.rsc.org/greenchem)

## Enhanced Catalytic Activity of Palladium Nanoparticles Confined inside Porous Carbon in Methanol Electro-Oxidation

Abheek Datta, Sutanu Kapri and Sayan Bhattacharyya\*

*Department of Chemical Sciences, Indian Institute of Science Education and Research (IISER) Kolkata, Mohanpur - 741246, India*

\* Email for correspondence: [sayanb@iiserkol.ac.in](mailto:sayanb@iiserkol.ac.in)

### Abstract:

The effects of confinement of Pd nanoparticles (NPs) inside hollow carbon matrices are evaluated based on their performance in methanol (MeOH) electro-oxidation (EOx). The performance of three catalyst systems were compared: 1) Pd NPs exclusively confined inside the hollow carbon NPs, 2) Pd NPs distributed between the pores and surface of porous carbon and 3) Pd NPs bound to the surface of activated charcoal. When NPs are exclusively confined, the electrocatalytic activity improves due to higher proximity of the NPs to the reactants inside the cavity and minimal leaching of the NPs over 300 cycles. NP confinement yields high anodic peak current density (AP-CD) of  $142 \text{ mA cm}^{-2}$  ( $626 \text{ cm}^2/\text{mg}_{\text{Pd}}$ ) at lower anodic potential of  $-0.3 \text{ V}$  and excellent re-usability, as compared to the partially confined and exposed NPs. A minimal loading of 1.2-2.5 wt% Pd NPs inside the mesoporous carbon resulted in high electrochemically active surface area (ECSA), which clearly underlines the positive effect of the confinement of metal NPs.

*Keywords:* Methanol electro-oxidation; Confinement; Nanoparticles; Mesoporous carbon; palladium

## INTRODUCTION

The high energy conversion efficiency and power density of direct MeOH fuel cells (DMFCs) makes them attractive to address the demand for clean and renewable energy.<sup>1</sup> DMFCs utilize MeOH EOX reaction and have easy storability and transport of MeOH, cost-effectiveness of the cell design and eco-friendly applications.<sup>2-4</sup> Different heterogeneous nanocatalysts with various morphologies are being explored for MeOH EOX in order to enhance the activity of DMFC.<sup>5,6</sup> In a confined geometry, embedding the catalyst NPs inside nanochannels or pores has potential to increase the catalytic performance of nanocatalysts.<sup>7,8</sup> The confinement effect on the catalyst NPs implies enhancement of catalytic activity as the confined space provides the ideal conditions to entrap the nanocatalyst particles, however providing the leeway for catalysis. In the last decade, metal NPs encapsulated within hollow nanostructures have generated a great deal of attention in heterogeneous catalysis.<sup>9-11</sup>

Among the confining supports, carbon nanomaterials are most popular because of their chemical stability, regenerability, mechanical strength, high porosity and ease of surface functionalization.<sup>12</sup> One dimensional carbon nanostructures such as tubes, fibers and whiskers,<sup>13,14</sup> along with nanospheres and cages,<sup>15</sup> are desirable host materials for anchoring and confining the catalyst NPs in heterogeneous catalysis reactions. However, the most commonly used support is mesoporous carbon because of their large surface area,<sup>16</sup> where the NPs can be embedded inside the pores or immobilized on the surface.<sup>17-24</sup> Among the catalyst NP systems, Pd NPs demonstrate excellent catalytic activity towards various heterogeneous catalysis reactions.<sup>25-28</sup> The Pd nanocatalysts are the best balance between cost-effectiveness and decent activity as compared to other metal NPs. The Pd NPs have versatile applicability as best alternative to expensive Pt in the fuel cells.<sup>4,29</sup> Although Pd NPs confined inside the carrier

support were tested in organic molecular transformations,<sup>30</sup> so far there is no report on the confinement effect of Pd NPs in electro-oxidation of alcohols.

In this context, encapsulating the Pd NPs within well-defined carbon nanostructures could enhance the activity of the nanocatalyst. Pd NPs are encapsulated inside the pores of carbon NPs and the performance of these confined electrocatalysts is enhanced in MeOH EOX. Two confined systems were synthesized. 150-200 nm Pd@C1 system was synthesized from Pd@SiO<sub>2</sub> by successive C-coating to Pd@SiO<sub>2</sub>@C and removal of SiO<sub>2</sub> template. The second partially confined Pd@C2 system was synthesized by encapsulating Pd NPs within carbonized sucrose, followed by annealing. The carbon confined Pd NPs exhibits excellent catalytic activity and reusability in comparison with a conventional Pd/C system comprising Pd NPs chemically immobilized on activated charcoal. The simple strategy of NP confinement may be generalized to other metal NPs confined inside various nanostructured supports for improved performance in fuel cells and other applications.<sup>22, 23</sup>

## RESULTS AND DISCUSSION

### Structural and Morphological Studies

The surface area and porosity measurement studies provide an insight into the structural evolution and confinement effects of the Pd@C1 catalyst. Figure 1a shows the N<sub>2</sub> adsorption-desorption curves and the pore characteristics, the parameters of which are tabulated in Table 1. The N<sub>2</sub> sorption curve of Pd@SiO<sub>2</sub> NPs exhibit type IV isotherm with H2 hysteresis loop showing the limiting uptake of adsorbate at high relative pressure ( $P/P_0$ ) which indicates the capillary condensation inside the 5-15 nm interconnected open mesopores in the SiO<sub>2</sub> shell.<sup>31,32</sup> After carbonization and annealing, the surface area reduces by 62% in Pd@SiO<sub>2</sub>@C due to

blocking of the SiO<sub>2</sub> pores by the carbon layer. Consequently the hysteresis loop changes to H1 type due to constriction of the pores, evident from much lower pore volume and very small pore size distribution. HF etching of SiO<sub>2</sub> leads to 3.3 times increase in surface area along with an increase in pore volume and broad pore size distribution in Pd@C1. The non-reversible Type II isotherm is indicative of both monolayer and multilayer adsorption. The hollow cavities created by HF treatment initially adsorb the N<sub>2</sub> molecules, followed by the appearance of a linear middle region in the sorption curve which shows the completion of monolayer adsorption and beginning of multilayer adsorption. In spite of the huge increase in surface area for Pd@C1, the slight increase in the total micropore volume can be attributed to graphitization and hence desensitization of the outermost carbon layer to N<sub>2</sub> adsorption after annealing at 900°C.<sup>33</sup> In fact the low pressure hysteresis is a signature of sub-nm wide pores associated with irreversible uptake of adsorbate (N<sub>2</sub>) molecules.<sup>25</sup> These Å-wide pores in the C-shell provide the percolation pathway for the KOH and methanol molecules to reach the confined Pd NPs for the latter's electro-oxidation. The N<sub>2</sub> sorption characteristics of Pd@C2 and Pd/C are presented in Figure 1b and Table 1. The commercial activated charcoal in Pd/C possesses a high surface area of 779 ± 5 m<sup>2</sup>/g, with pores of diameter 3.8 and 9.2 nm, whereas the Pd@C2 has a comparatively lesser surface area of 302 ± 1 m<sup>2</sup>/g. The Pd NPs confined inside the bulk of Pd@C2 have access to the reactant molecules through open 3.4 nm pores as well as the sub-nm pores.

The field emission scanning electron microscopy (FESEM) images and elemental analyses (Figure 2a-j) reveal the structural properties of Pd@C1. After carbonization and annealing of ~22 nm Pd@SiO<sub>2</sub> NPs, 180-200 nm Pd@SiO<sub>2</sub>@C particles were obtained. HF treatment of Pd@SiO<sub>2</sub>@C particles breaks the continuous C-layer of Pd@SiO<sub>2</sub>@C resulting in well-defined 150-180 nm Pd@C1 particles with uneven surface and 0.8 wt% leftover SiO<sub>2</sub>

(Figure 2g-i). Pd  $L\alpha_1$  mapping in Figure 2j shows the uniform distribution of Pd NPs. In the absence of  $\text{SiO}_2$  template in Pd@C2, the Pd NPs are not perfectly confined since a large fraction of the NPs (arrows in Figure 2k) reside on the carbon surface. Figure 2m indicates the distribution of Pd NPs both inside (weaker dots) and outside (brighter dots) the mesoporous matrix. The partial NP confinement in Pd@C2 emphasizes the importance of  $\text{SiO}_2$  template to generate catalyst NPs exclusively confined inside C-matrices of well-defined morphologies. The third Pd/C sample has Pd NPs uniformly dispersed over the surface of activated charcoal as observed in Figure 2m. The average Pd wt% in Pd@C1, Pd@C2 and Pd/C was found to be 1.2, 2.4 and 2.5, respectively by energy dispersive X-ray spectral (EDS) analyses.

Transmission electron microscopy (TEM) images corroborate the morphologies observed in FESEM. Figure 3a shows the transmission electron micrograph (TEM) of a single  $5.3 \pm 0.2$  nm Pd NP inside the  $\text{SiO}_2$  shell. The inter-linked Pd@ $\text{SiO}_2$  NPs appear  $\sim 50$  nm in diameter (Figure 3b). The arrows in Figure 3b indicate the dispersed Pd NPs inside the  $\text{SiO}_2$  matrix. Individual mesoporous  $\sim 165$  nm Pd@C1 particles with colonized  $\sim 8.5$  nm Pd NPs inside the mesopores are observed in Figure 3 c, d. The increase in size of the Pd NPs by  $\sim 3$  nm was due to annealing at  $900^\circ\text{C}$ . The selected area electron diffraction (SAED) pattern in Figure 3e shows the Pd (111) and (200) reflections. At  $900^\circ\text{C}$ , carbon becomes partially graphitic. The  $d$ -spacing of 0.5 nm can result from the regions of high curvature of the immediate carbon layers surrounding each Pd NP.<sup>34</sup> The SAED pattern is duly supported by the powder X-ray diffraction (PXRD) patterns of Pd@ $\text{SiO}_2$  and Pd@C1 in Figure 3f. The peak at  $22.5^\circ$  in Figure 3f(1) represents the amorphous  $\text{SiO}_2$  shell. The crystallite size of Pd NPs obtained from the PXRD peak broadening using Debye Scherrer's equation was 8.2 nm, which correlates well with the size of Pd NPs in Pd@C1. Although PXRD patterns do not provide evidence of any  $\text{Pd}^{2+}$ , the presence of a minor

fraction of amorphous PdO is most likely.<sup>25</sup> Peak fitting of the X-ray photoelectron spectrum (XPS) of the Pd *3d* level of Pd@C1 (Figure S1, Supporting Information) shows the presence of 35% Pd<sup>2+</sup> species. The metallic nature of the Pd NPs could be retained due to annealing under N<sub>2</sub>. The 12-16 nm pores of Pd@C2 are clearly observed in Figure 3g. The dispersed Pd NPs on activated charcoal in Pd/C can be visualized from the dark spots on the carbon matrix in Figure 3h.

The chemical bonding characteristics of Pd@C1 at different stages of synthesis was studied by fourier transform infrared (FTIR) spectroscopy and the spectra are presented in Figure 4. For Pd@SiO<sub>2</sub> and Pd@SiO<sub>2</sub>@C, the wavenumber and intensity of the peaks are similar indicating no major change in the bonding after carbonization. The 3420 cm<sup>-1</sup> peak is due to O-H stretching from adsorbed moisture and the peak at 2945 cm<sup>-1</sup> arises from Si-CH<sub>2</sub> stretching due to bonding interactions between cetrimonium bromide (CTAB) surfactant molecules on the surface of Pd NPs and the overlying SiO<sub>2</sub>. The peaks at 1654 and 1440 cm<sup>-1</sup> are the N-CH<sub>3</sub> stretching vibrations of CTAB.<sup>35</sup> The 1085, 950 and 882 cm<sup>-1</sup> peaks account for Si-O-Si stretching in TO<sub>3</sub>, TO<sub>2</sub> and TO<sub>1</sub> modes respectively.<sup>36</sup> The absence of all the above peaks except a weaker O-H stretching at 3420 cm<sup>-1</sup> in Pd@C1 confirms complete removal of CTAB after annealing at 900°C and SiO<sub>2</sub> after HF treatment.

### Electrocatalytic Activities

Mesoporous carbon without Pd NP loading showed a peak current density 0.9 mA/cm<sup>2</sup> (Figure S2). The catalytic activity of mesoporous carbon probably arises from a large fraction of defect sites and ECSA was observed to be 1.71 cm<sup>2</sup>/mg<sub>Carbon</sub>.<sup>37</sup> Figure 5 presents the cyclic voltammograms (CVs) for MeOH EOx using the heterogeneous catalysts coated on glassy

carbon electrodes and the parameters are tabulated in Table 2. The ECSA of the catalyst systems are compared with other reports.<sup>2,4,21,38-43</sup> The solutions were stirred at 250 rpm to evenly distribute the MeOH to the electrode surface, remove concentration gradient of OH<sup>-</sup> ions and to prevent accumulation of the oxidation products on the electrode surface resulting in a fast decrease in the anodic potential and high catalytic activity (Table S3). It is clearly observed from Figure 5a that the peak of the anodic oxidation remains at -0.30 to -0.25 V versus saturated calomel electrode (SCE). The corresponding AP-CD of Pd@C1 is 1.4 and 2 times higher than that for Pd@C2 and Pd/C catalysts, respectively. The utility of NP confinement and the superior activity of Pd@C1 were also prominent from the performance of the electrocatalysts in the recyclability tests up to 300<sup>th</sup> cycle (Figure 5b, c). After 200<sup>th</sup> electro-oxidation cycle, the confined catalyst Pd@C1 shows decent activity with the AP-CD of 100 mA cm<sup>-2</sup> (176 cm<sup>2</sup>/mg<sub>Pd</sub>). The re-usability of Pd@C2 was comparatively lower. In contrast, the activity of Pd/C was lost after the 200<sup>th</sup> cycle. Interestingly, AP-CD of Pd@C1 and Pd@C2 was still maintained after the 300<sup>th</sup> cycle. The performance of Pd@C1 is comparatively better than the recently reported catalyst nanosystems used for MeOH EOX (Table 2).<sup>3,4,38-41,44,45</sup> The anodic peak potential was observed at one of the lowest reported value of ~ -0.3 V,<sup>45</sup> whereas the AP-CD of 142 mA cm<sup>-2</sup> (626 cm<sup>2</sup>/mg<sub>Pd</sub>) is the highest among the reported Pd NP catalysts. Figure 5d shows the change in AP-CD of Pd@C1 for MeOH EOX with increasing pH of the solution. It was observed that with 0.5 M MeOH, the AP-CD increased from 70/80 (297/322 cm<sup>2</sup>/mg<sub>Pd</sub>) to 142/141 mA cm<sup>-2</sup> (626/613 cm<sup>2</sup>/mg<sub>Pd</sub>) with/without stirring for increasing pH from 0.1 to 0.5 M KOH, respectively (Table S3). The MeOH EOX occurs simultaneously with the oxidation of the Pd NPs and the competition of adsorption of MeOH and OH<sup>-</sup> on the NP surface. Higher pH increases the concentration of both chemically and physically adsorbed active OH<sup>-</sup> on the NP

surface which enhances AP-CD.<sup>46</sup> However, with 1 M KOH, AP-CD slightly decreased to 135 mA cm<sup>-2</sup> (607 cm<sup>2</sup>/mg<sub>Pd</sub>). Again, by altering the MeOH concentration keeping 0.5 M KOH, the AP-CD of Pd@C1 increases from 76/103 mA cm<sup>-2</sup> (357/378 cm<sup>2</sup>/mg<sub>Pd</sub>) for 0.1 M to 142/141 mA cm<sup>-2</sup> (626/613 cm<sup>2</sup>/mg<sub>Pd</sub>) for 0.5 M MeOH and decreases to 120/133 mA cm<sup>-2</sup> (591/603 cm<sup>2</sup>/mg<sub>Pd</sub>) for 1 M MeOH with/without stirring (Figure 5e and (Table S4). Increasing the MeOH concentration beyond 0.5 M results in chances of MeOH crossover across the permeable Nafion layer posing multiple mass transport issues.<sup>47,48</sup> Optimizing the MeOH concentration to reduce its crossover is always a challenge. In this study, 0.5 M KOH and 0.5 M MeOH were found to be optimum.

The morphology of the catalyst systems after the electro-oxidation cycles is shown in Figure 6. After 200 cycles of MeOH EOX, the core-shell structure of Pd@C1 disintegrates, however the Pd NPs were observed to be trapped within the carbon matrix. The Pd NPs aggregated after continued cycles and ~40 nm diameter NPs are observed after 200 cycles in Figure 6b. The elemental line scan over a selected area of the used Pd@C1 shows a prominent Pd signal indicating decent anchoring of the NPs. After 300 cycles, the core-shell structure of Pd@C1 completely breaks, however Pd NPs are still observed correlating the ECSA (24 m<sup>2</sup>/mg<sub>Pd</sub>) after 300 cycles. The morphology of Pd@C2 after 200 cycles consists of scattered mass of Pd and C along with carbon shells. These shells rupture after 300 cycles. Elemental line scan (Figure 6h) shows the presence of Pd NPs, although the relative content of Pd is much lower than that of Pd@C1 after 300 cycles (Figure 6e). The morphologies of Pd/C after 200 and 300 cycles are similar and the elemental analysis in (Figure 6k) shows the presence of negligible Pd after 300 cycles of MeOH EOX. Figure 7 shows a cartoon view of the performance of the three catalysts. Although, the confinement of NPs in the mesopores of the carbon support of

Pd@C1 indeed can lead to enhancement of the catalytic activity and stability by providing excellent anchoring possibilities, there is also a trade off in this effect. The confinement can hinder decent fuel diffusion and lead to kinetic problems in the MeOH EOX process. Also diffusion of surrounding carbon can cause deactivation of catalyst. However, the 20 nm and Å-wide pores come to the rescue and allow intake of the fluid inside the cavity containing the NPs, and thus better contact could be established between the trapped reactant molecules and the confined catalyst NPs. In Pd@C1, MeOH, KOH and H<sub>2</sub>O come in contact with the Pd NPs after percolating through the open pores at the wall of the hollow cavity. It is noteworthy that Pd@C1 with Pd NPs half the wt% to that of Pd@C2 and Pd/C could perform better MeOH EOX. Actually, the normal Pd NP loading used in scientific studies and commercial catalysts are at least ~20 wt%. In Pd@C1, since the Pd NPs are exclusively confined inside the mesopores, the Pd loading is expectedly low. In spite of doubling the Pd NP loading in Pd@C2 and Pd/C, the electrocatalytic activities were lower as compared to Pd@C1, which clearly underlines the positive influence of the confinement of metal NP catalyst. Confinement of the NPs has several advantages such as minimal surface oxidation after prolonged electrocatalytic cycles, zero leaching from inside the hollow cavity and increased redox properties of the confined NPs due to greater electron density.<sup>49,50</sup> The above factors ensure better mass transport around the NPs and smaller electrical resistance, which provides better AP-CD. The drop in AP-CD after repeated cycles could be due to limited surface oxidation of the NPs after prolonged use and the OH<sup>-</sup> ions from abundant H<sub>2</sub>O adsorbed on the surface of Pd NPs which competes with the OH<sup>-</sup> in solution.<sup>47</sup> When the Pd NPs are partially confined and the rest exposed to the surface of mesoporous carbon as in Pd@C2, the Pd NPs at the surface become vulnerable to oxidation and leaching. With continued cycles, even if the confined NPs experience lesser surface oxidation,

the exposed NPs become increasingly oxidized and AP-CD also decreases. In Pd/C, the chances of surface oxidation and leaching are the highest decreasing its activity. The moisture content of Pd@C1, Pd@C2 and Pd/C after the 200<sup>th</sup> cycle was estimated to be 14.7, 10.3 and 7.9 wt%, which after the 300<sup>th</sup> cycle reduced to 12.9, 7.6 and 2.1 wt%, respectively. The excess moisture in Pd@C1 indicates that both MeOH and KOH are trapped inside the hollow cavity, justifying its superior activity. Solid state UV-visible spectra in Figure 5f show the absorbance of MeOH present in the three catalysts and the shift of the peaks signifies modifications in the ground and excited states due to molecular interactions such as hydrogen bonding.<sup>51</sup> The left-over MeOH in Pd@C1 and Pd@C2 is mostly from those trapped under confinement, whereas in Pd/C, the left-over MeOH is solely from inside the pores of activated charcoal. Inside the hollow cavity, the trapped MeOH molecules will have free OH<sup>-</sup> sites, whereas inside the nm- and Å-sized pores, the molecules will have larger tendency to self-organize via hydrogen bonding. Thus from Pd@C1 to Pd@C2 and Pd/C, an intensity decrease in the absorption due to self-aggregation and a blue-shift due to loss of terminal free OH<sup>-</sup> groups is observed.

## Conclusions

In summary, we have shown that confining the NP catalysts inside well-defined hollow carbon structures can significantly enhance the activity of the catalyst in MeOH EOx as compared to the partially confined and exposed NP catalysts. According to our literature survey, this is the first report on the confinement effect of NP catalysts in MeOH EOx, which also provides a significantly high AP-CD of 142 mA cm<sup>-2</sup> (626 cm<sup>2</sup>/mg<sub>Pd</sub>) as compared to other Pd NP catalyst systems. The adapted and highly efficient process of Pd@C1 may be applicable to prepare various metal NPs confined within supports.

## Experimental Section

**Materials:** Tetraethyl orthosilicate (TEOS,  $\text{Si}(\text{OC}_2\text{H}_5)_4$ , Merck India, synthesis grade), CTAB (Sigma Aldrich, 98%), potassium tetrachloropalladate ( $\text{K}_2\text{PdCl}_4$ , Arora Matthey Limited), polyvinylpyrrolidone (PVP, Loba Chemie, Mol. Wt. 40,000), ethanol (absolute for analysis, Merck India), ammonium hydroxide (25%, EMPLURA, Merck India), hydrofluoric acid (HF, Merck, 40%), sucrose (pure grade, Merck India), hydrochloric acid (HCl, 35% Merck India), MeOH (EMPLURA, Merck India), potassium hydroxide pellets (EMPLURA, Merck India) and activated charcoal (Merck India) were used without further purification.

**Characterization:** The surface area and porosity measurements were carried out with a Micromeritics Gemini VII surface area analyzer. The nitrogen adsorption/desorption isotherms were reported by BJH (Barret-Joyner-Halenda) surface/volume mesopore analysis. The micropore volume was calculated using the Frenkel-Halsey-Hill isotherm equation. Each sample was degassed at  $300^\circ\text{C}$  for 2 h. FESEM images were obtained in Carl Zeiss SUPRA 55VP FESEM. EDAX studies were performed with the Oxford Instruments X-Max with INCA software coupled to the FESEM. TEM images were recorded by UHR-FEG-TEM, JEOL, JEM 2100 F model using 200 kV electron source. The XRD measurements were performed with a Rigaku (mini flex II, Japan) powder X-ray diffractometer having  $\text{Cu K}\alpha = 1.54059 \text{ \AA}$  radiation. XPS measurements were performed on the samples mounted on copper stubs with silver paste, using  $\text{Al K}\alpha$  radiation (1486.6 eV) in a commercial photoelectron spectrometer from VSW Scientific Instruments. The base pressure of the chamber was maintained around  $5 \times 10^{-10}$  mbar during the experiments. The Fourier transform infrared (FTIR) studies were performed with a Perkin Elmer spectrum RX1 with KBr pellets. Ultraviolet-visible absorption spectra were collected using a JASCO V-670 spectrophotometer. Moisture % in the samples were measured using a Sartorius MA-150 analyzer by heating the samples up to  $200^\circ\text{C}$ .

**Materials Synthesis:**

*Synthesis of Pd NPs:* Pd NPs were synthesized as reported by Narayanan *et al.*<sup>52</sup> with slight modifications. The palladium precursor solution was prepared by adding 0.16 g anhydrous  $K_2PdCl_4$  with 6 mL of 0.2M HCl and diluting it to 250 mL with de-ionized water. 15 mL of this precursor solution, 21 mL of de-ionized water, 0.0067 g of PVP and 2 drops of 1M HCl were mixed together and heated. 15 mL ethanol was added to the mixture at the initial stages of refluxing, continued for 3 h. Upon completion of the reaction, a dark brown colloid of Pd NPs was collected.

**Preparation of Pd@C1:**

*Synthesis of Pd@SiO<sub>2</sub> (Step 1):* The colloidal solution of Pd NPs was re-dispersed in a solution of 5 vol%  $NH_4OH$  in ethanol. Soon after, 15 mL 10 vol% TEOS in ethanol and 0.05 g CTAB were mixed with 10 mL of re-dispersed Pd NP solution. The mixture was kept under constant stirring at 600 rpm for 4 h. Upon completion of the reaction, the product was filtered and washed thrice with distilled water and ethanol followed by drying at 70°C for 3 h.

*Carbonization of Pd@SiO<sub>2</sub> (Step 2):* 0.3 g of dried as-prepared Pd@SiO<sub>2</sub> sample was dispersed in 10 mL ethanol and 20 mL of 0.5 M aqueous solution of sucrose was added to it. After adding 5 ml of 2 M HCl to this mixture, it was refluxed for 6h and cooled to room temperature. A dark brown colloid was obtained as product, which was collected using rotary evaporator by evaporating the solvent, washed with ethanol and dried, followed by annealing at 900°C for 2h under  $N_2$ . Upon completion of the annealing and cooling, the grey powder of Pd@SiO<sub>2</sub>@C was collected.

*Removal of SiO<sub>2</sub> (Step 3):* The powdered sample of Pd@SiO<sub>2</sub>@C was added to 10 mL of 5 vol% HF in water and sonicated for 2h. After SiO<sub>2</sub> was etched out, the solid was filtered and washed with ethanol and distilled water thrice followed by drying at 70°C for 3h.

***Preparation of Pd@C2:***

30 mL of the colloidal Pd NP solution was mixed with 20 mL of 0.5 M aqueous solution of sucrose. After adding 5 ml of 2 M HCl to this mixture, it was refluxed for 6 h and cooled to 25°C. A dark brown colloid was obtained as product, which was collected by evaporating the solvent, washed with ethanol and dried followed by annealing at 900°C for 2h in inert atmosphere. Upon completion of the annealing and cooling, the black powder of Pd@C2 was collected.

***Preparation of Pd/C catalyst:***

The conventional catalyst where Pd NPs are anchored on the surface of activated charcoal was prepared as follows. 0.1 g of activated charcoal, 0.0067 g of PVP, 15 ml of previously prepared K<sub>2</sub>PdCl<sub>4</sub> solution and 21 ml de-ionized water were mixed together and the mixture was stirred for 0.5 h at room temperature. Afterwards the mixture was heated with constant stirring at 600 rpm. When the solution began to reflux, 15 ml of ethanol was added to it and kept under refluxing condition for 3 h. After the reaction was complete, the solid product was filtered out and washed thrice with ethanol and distilled water followed by drying at 70°C for 3 h.

***Electrochemical Measurements:*** Electrocatalytic activities of the catalyst samples were measured with a conventional three electrode cell in a CHI604D electrochemical workstation. The three electrode cell was assembled by using a Pt wire as counter electrode, a saturated

calomel electrode (SCE) as reference electrode and a glassy carbon (GC) disk (3 mm diameter) coated with the catalyst as working electrode. The working electrode was designed as follows: 1 mg of powdered catalyst was dispersed in a mixed solution containing 250  $\mu\text{L}$  distilled water, 250  $\mu\text{L}$  of ethanol and 25  $\mu\text{L}$  of 5% aqueous Nafion solution. 5  $\mu\text{L}$  of the resulting suspension was carefully drop casted on to the surface of GC disk followed by drying at 25°C for 0.5 h. All electrochemical measurements were performed without and with mechanical stirring at 250 rpm. The scanning rate was maintained constant at 50  $\text{mVs}^{-1}$ .

### Acknowledgements

The Department of Science and Technology (DST), Government of India is duly acknowledged for the financial support under grant no. SR/S1/PC-28/2011. The authors thank Prof. S. M. Shivaprasad, JNCASR India for the XPS measurement. AD and SK thank University Grants Commission (UGC) and Council of Scientific and Industrial Research (CSIR), New Delhi for their fellowships, respectively.

### References:

- 1 S. K. Kamarudin, F. Achmad and W. R. W. Daud, *Int. J. Hydrogen Energ.*, 2009, **34**, 6902-6916.
- 2 Y. Lu, Y. Jiang, H. Wu and W. Chen, *J. Phys. Chem. C*, 2013, **117**, 2926–2938.
- 3 L. Zhao, J. P. Thomas, N. F. Heinig, M. Abd-Ellah, X. Wang and K. T. Leung, *J. Mater. Chem. C*, 2014, **2**, 2707–2714.
- 4 M. Zhao, K. Abe, S. Yamaura and Y. Yamamoto, *Chem. Mater.*, 2014, **26**, 1056–1061.
- 5 S. Guo, S. Dong and E. Wang, *Chem. Commun.*, 2010, **46**, 1869–1871.
- 6 G. Lu and A. Wieckowski, *Curr. Opin. Colloid Interface Sci.*, 2000, **5**, 95-100.
- 7 J. Zhang, S. Guo, J. Wei, Q. Xu, W. Yan, J. Fu, S. Wang, M. Cao and Z. Chen, *Chem. Eur. J.*, 2013, **19**, 16087 – 16092.

- 8 N. A. M. Barakat, M. A. Abdelkareem, A. Yousef, S. S. Al-Deyab, M. El-Newehy and H. Y. Kim, *Int. J. Hydrogen Energ.*, 2013, **38**, 3387-3394.
- 9 D. Wang, G. Yang, Q. Ma, M. Wu, Y. Tan, Y. Yoneyama and N. Tsubaki, *ACS Catal.*, 2012, **2**, 1958–1966.
- 10 D. Deng, L. Yu, X. Chen, G. Wang, L. Jin, P. Pan, J. Deng, G. Sun and X. Bao, *Angew. Chem. Int. Ed.*, 2013, **52**, 371–375.
- 11 Y. Liu, W. Zhang, S. Li, C. Cui, J. Wu, H. Chen and F. Huo, *Chem. Mater.*, 2014, **26**, 1119–1125.
- 12 F. Rodríguez-Reinoso, *Carbon*, 1998, **36**, 159-175.
- 13 Z. Chen, Z. Guan, M. Li, Q. Yang and C. Li, *Angew. Chem. Int. Ed.*, 2011, **50**, 4913–4917.
- 14 A. Datta, P. Dutta, A. Sadhu, S. Maiti and S. Bhattacharyya, *J. Nanopart. Res.*, 2013, **15**, 1808-(1-15).
- 15 G. Wang, J. Hilgert, F. H. Richter, F. Wang, H. Bongard, B. Spliethoff, C. Weidenthaler and F. Schüth, *Nat. Mater.*, 2014, **13**, 293-300.
- 16 K. Ha, G. Kwak, K. Jun, J. Hwang and J. Lee, *Chem. Commun.*, 2013, **49**, 5141-5143.
- 17 S. Bhattacharyya and A. Gedanken, *J. Phys. Chem. C*, 2008, **112**, 659-665.
- 18 S. Bhattacharyya, A. Gabashvili, N. Perkas and A. Gedanken, *J. Phys. Chem. C*, 2007, **111**, 11161-11167.
- 19 B. Fıçıcılar, A. Bayrakçeken and I. Eroğlu, *J. Power Sources*, 2009, **193**, 17-23.
- 20 H. Wang, X. Bo, J. Bai, L. Wang and L. Guo, *J. Electroanal. Chem.*, 2011, **662**, 281-287.
- 21 G. Z. Hu, F. Nitze, X. Jia, T. Sharifi, H. R. Barzegar, E. Gracia-Espino and T. Wagberg, *RSC Adv.*, 2014, **4**, 676-682.
- 22 R. Ryoo, S. H. Joo, M. Kruk and M. Jaroniec, *Adv. Mater.* 2001, **13**, 677-681.
- 23 O. David, W. J. N. Meester, H. Bieräugel, H. E. Schoemaker, H. Hiemstra and J. H. Van Maarseveen, *Angew Chem. Int. Ed.* 2003, **42**, 4373-4375.
- 24 G. Hu, F. Nitze, E. Gracia-Espino, J. Ma, H. R. Barzegar, T. Sharifi, X. Jia, A. Shchukarev, L. Lu, C. Ma, G. Yang and T. Wågberg, *Nature Commun.* 2014, **5**, 5253.
- 25 A. Datta, A. Sadhu, S. Santra, S. M. Shivaprasad, S. K. Mandal and S. Bhattacharyya, *Chem. Commun.*, 2014, **50**, 10510-10512.

- 26 A. Balouch, A. A. Umar, A. A. Shah, M. M. Salleh and M. Oyama, *ACS Appl. Mater. Interfaces*, 2013, **5**, 9843–9849.
- 27 Y. Huang, Z. Lin and R. Cao, *Chem. Eur. J.*, 2011, **17**, 12706 – 12712.
- 28 M. S. Kwon, N. Kim, C. M. Park, J. S. Lee, K. Y. Kang and J. Park, *Org. Lett.*, 2005, **7**, 1077-1079.
- 29 E. Antolini, *Energy Environ. Sci.*, 2009, **2**, 915–931.
- 30 M. Zhao, K. Deng, L. He, Y. Liu, G. Li, H. Zhao and Z. Tang, *J. Am. Chem. Soc.*, 2014, **136**, 1738-1741.
- 31 K. S. W. Sing, D. H. Everett, R. A. W. Haul, L. Moscou, R. A. Pierotti, J. Rouquérol and T. Siemieniowska, *Pure & Appl. Chem.*, 1985, **57**, 603-619.
- 32 S. Kubo, R. J. White, N. Yoshizawa, M. Antonietti and M-M. Titirici, *Chem. Mater.*, 2011, **23**, 4882-4885.
- 33 Y. Gogotsi, A. Nikitin, H. Ye, W. Zhou, J. E. Fischer, B. Yi, H. C. Foley and M. W. Barsoum, *Nat. Mater.*, 2003, **2**, 591-594.
- 34 Y. Gogotsi, *Carbon Nanomaterials*, CRC Press & Francis Group, Boca Raton, 2006, p. 164.
- 35 R. B. Viana, A. B. F. da Silva and A. S. Pimentel, *Adv. Phys. Chem.*, 2012, **2012**, 903272.
- 36 J. Osswald and K. T. Fehr, *J. Mater. Sci.*, 2006, **41**, 1335-1339.
- 37 G. Hu, F. Nitze, T. Sharifi, H. R. Barzegar and T. Wågberg, *J. Mater. Chem.* 2012, **22**, 8541-8548.
- 38 H. Huang and X. Wang, *J. Mater. Chem.*, 2012, **22**, 22533–22541.
- 39 Y. Liu, M. Chi, V. Mazumder, K. L. More, S. Soled, J. D. Henao and S. Sun, *Chem. Mater.*, 2011, **23**, 4199–4203.
- 40 Y. -W. Lee, A. -R. Ko, S. -B. Han, H. -S. Kim, D. -Y. Kim, S. -J. Kim and K. -W Park, *Chem. Commun.*, 2010, **46**, 9241–9243.
- 41 X. Wang, W. Wang, Z. Qi, C. Zhao, H. Ji and Z. Zhang, *Electrochem. Commun.*, 2009, **11**, 1896-1899.
- 42 H. Wu, H. Li, Y. Zhai, X. Zu and Y. Jin, *Adv. Mater.*, 2012, **24**, 1594-1597.
- 43 S. Guo, S. Dong and E. Wang, *Chem. Commun.*, 2010, **46**, 1869-1871.

- 44 Z. J. Mellinger, T. G. Kelly and J. G. Chen, *ACS Catal.*, 2012, **2**, 751–758.
- 45 P. K. Shen, Z. Yan, H. Meng, M. Wu, G. Cui, R. Wang, L. wang, K. Si and H. Fu, *RSC Advances*, 2011, **1**, 191–198.
- 46 B. Ballarin, A. Mignani, E. Scavetta, M. Giorgetti, D. Tonelli, E. Boanini, C. Mousty and V. Prevot, *Langmuir*, 2012, **28**, 15065–15074.
- 47 S. Yan, S. Zhang, Y. Lin and G. Liu, *J. Phys. Chem. C*, 2011, **115**, 6986–6993.
- 48 T. S. Zhao, C. Xu, R. Chen and W. W. Yang, *Prog. Energy Combust. Sci.*, 2009, **35**, 275-292.
- 49 W. Chen, Z. Fan, X. Pan and X. Bao, *J. Am. Chem. Soc.*, 2008, **130**, 9414-9419.
- 50 S. Guo, X. Pan, H. Gao, Z. Yang, J. Zhao and X. Bao, *Chem. Eur. J.*, 2010, **16**, 5379 – 5384.
- 51 Y. Morisawa, A. Ikehata, N. Higashi and Y. Ozaki, *Chem. Phys. Lett.*, 2009, **476**, 205-208.
- 52 R. Narayanan and M. A. El-Sayed, *J. Am. Chem. Soc.*, 2003, **125**, 8340-8347.

**Table 1:** BET surface area ( $S_{\text{BET}}$ ), total pore volume ( $V_{\text{total}}$ ) and pore diameter (D) of the samples.

Sample	$S_{\text{BET}}$ ( $\text{m}^2/\text{g}$ )	$V_{\text{total}}$ ( $\text{cm}^3/\text{g}$ )	D (nm)
Pd@SiO <sub>2</sub>	520 ± 3	0.86 ± 0.01	9.5 (sharp)
Pd@SiO <sub>2</sub> @C	198 ± 3	0.480 ± 0.005	2.5 (weak)
Pd@C1	653 ± 3	0.6 ± 0.03	20.0 (broad)
Pd@C2	302 ± 1	0.02	3.4
Pd/C	779 ± 2	0.2 ± 0.03	3.8 (sharp), 9.2 (broad)

**Table 2:** Peak voltage in the 1<sup>st</sup> cycle ( $V_{1(\text{peak})}$ ), AP-CD in the 1<sup>st</sup> cycle ( $i_1$ ), after increased cycles for MeOH EOX with stirring the solution ( $i_{\text{cycles}}$ ), ECSA in the 1<sup>st</sup> cycle and ECSA<sub>cycles</sub> after increased cycles for MeOH EOX. The reactant concentrations in molarity are mentioned for  $n$  (NaOH) and  $h$  (MeOH).

Sample	$n + h$ (M)	$V_{1(\text{peak})}$ (V)	$i_1$ (mA/cm <sup>2</sup> )	ECSA (cm <sup>2</sup> /mg <sub>Pd</sub> )	$i_{\text{cycles}}$ (mA/cm <sup>2</sup> )	ECSA <sub>cycles</sub> (cm <sup>2</sup> /mg <sub>Pd</sub> )
Pd@C1	0.5 <i>n</i> +	-0.29	142	626	128 <sub>100</sub>	516 <sub>100</sub>
	0.5 <i>h</i>		141**	613*	100 <sub>200</sub>	404 <sub>200</sub>
Pd@C2	0.5 <i>n</i> +	-0.30	100	234	29 <sub>300</sub>	139 <sub>300</sub>
	0.5 <i>h</i>		120**	191*	85 <sub>100</sub>	202 <sub>100</sub>
						72 <sub>200</sub>
Pd/C	0.5 <i>n</i> +	-0.25	70	162	10 <sub>300</sub>	22 <sub>300</sub>
	0.5 <i>h</i>		108**	189*	41 <sub>100</sub>	95 <sub>100</sub>
Pt-Pd NPs/Reduced graphene oxide <sup>2</sup>	0.5 <i>n</i> +	0.7	120	197	3 <sub>200</sub>	7.6 <sub>200</sub>
	0.5 <i>h</i>				1 <sub>300</sub>	2.2 <sub>300</sub>
Pd-Ni-P NPs/C <sup>4</sup>	0.5 <i>n</i> + 1.0 <i>h</i>	0.7	~0.6	629	~0.7 <sub>400</sub>	—
Pd NPs on ordered mesoporous carbon <sup>X3</sup>	0.5 <i>n</i> + 1.0 <i>h</i>	-0.25	180/mg <sub>Pd</sub>	520	—	—
Pd NP/Low- defect graphene <sup>32</sup>	0.5 <i>n</i> + 1.0 <i>h</i>	-0.1	26.7	830	—	—
Pd <sub>34</sub> Pt <sub>66</sub> NPs <sup>34</sup>	0.1 <i>n</i> + 0.1 <i>h</i>	0.68	55	700	—	—
Pd NP/ WC <sup>35</sup>	1.0 <i>n</i> + 2.0 <i>h</i>	-0.1	1.4	227	—	—
Porous Pd NPs <sup>36</sup>	1.0 <i>n</i> + 0.5 <i>h</i>	-0.1	120	230	—	—
Pd NP based Nano- membrane <sup>X8</sup>	0.5 <i>n</i> + 1.0 <i>h</i>	-0.15	60/mg <sub>Pd</sub>	573	—	—
Pt-Pd nanowire <sup>X9</sup>	0.5 M H <sub>2</sub> SO <sub>4</sub> + 0.5 <i>h</i>	0.7	50	907	—	—

\*Without stirring.

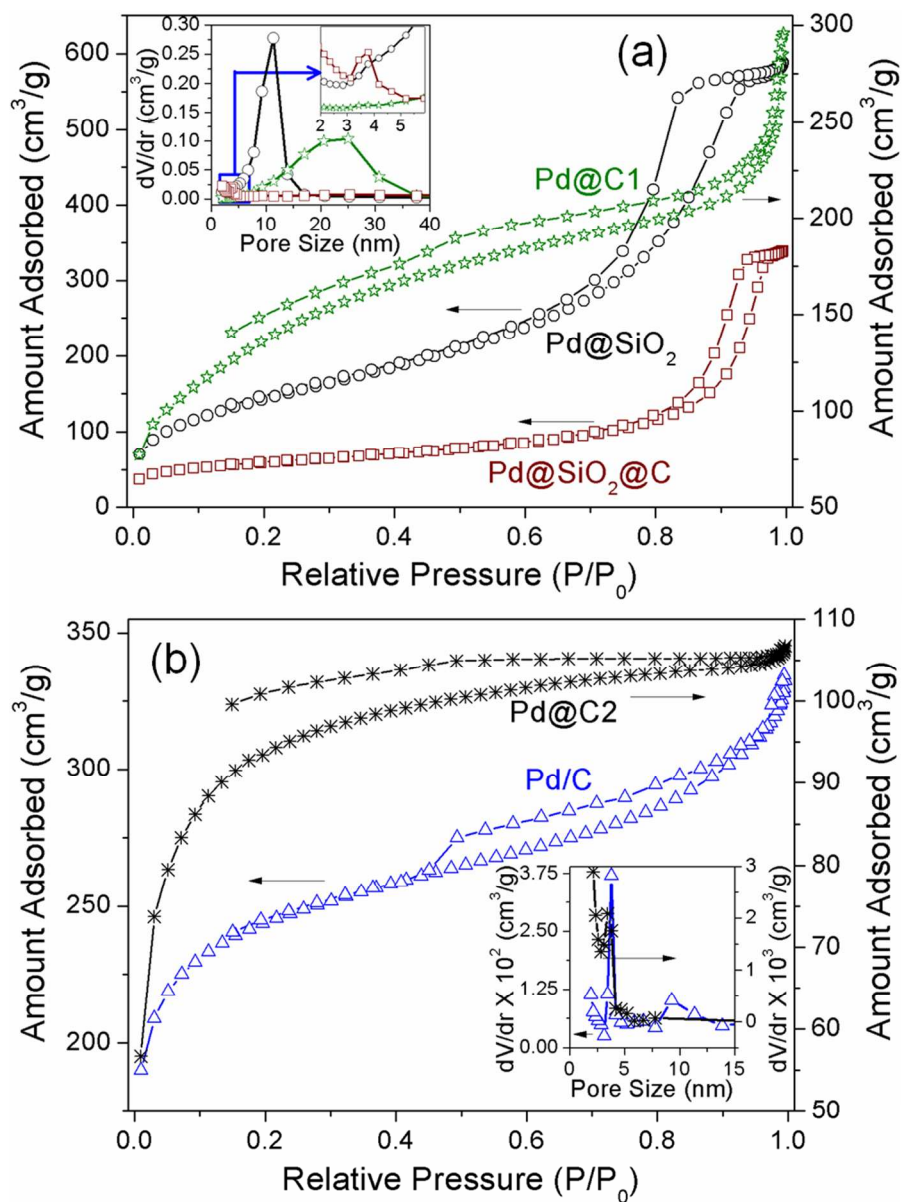


**Figure 1:**  $N_2$  sorption isotherms and (inset) pore size distributions.

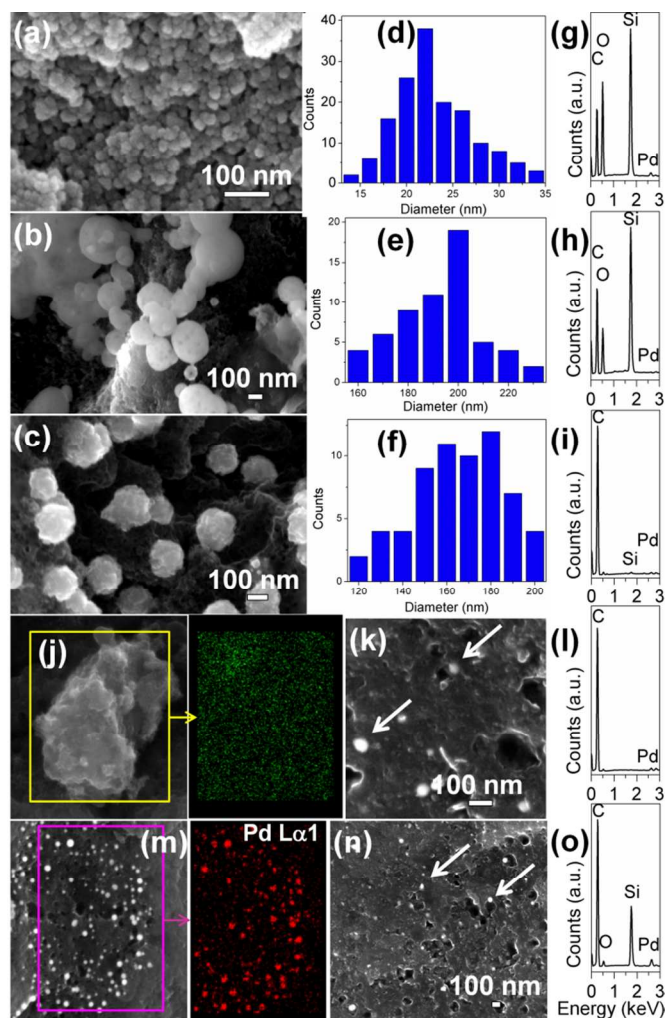


**Figure 2:** FESEM images of (a) Pd@SiO<sub>2</sub>, (b) Pd@SiO<sub>2</sub>@C, (c) Pd@C1, diameter histograms of (d) Pd@SiO<sub>2</sub>, (e) Pd@SiO<sub>2</sub>@C, (f) Pd@C1 and EDS spectra of (g) Pd@SiO<sub>2</sub>, (h) Pd@SiO<sub>2</sub>@C, (i) Pd@C1. (j) Elemental mapping of Pd Lα1 over a selected region of Pd@C1. (k) FESEM image of Pd@C2 and (l) its EDS spectrum. (m) Elemental mapping of Pd Lα1 over a selected region of Pd@C2. (n) FESEM image of Pd/C and (o) its EDS spectrum.

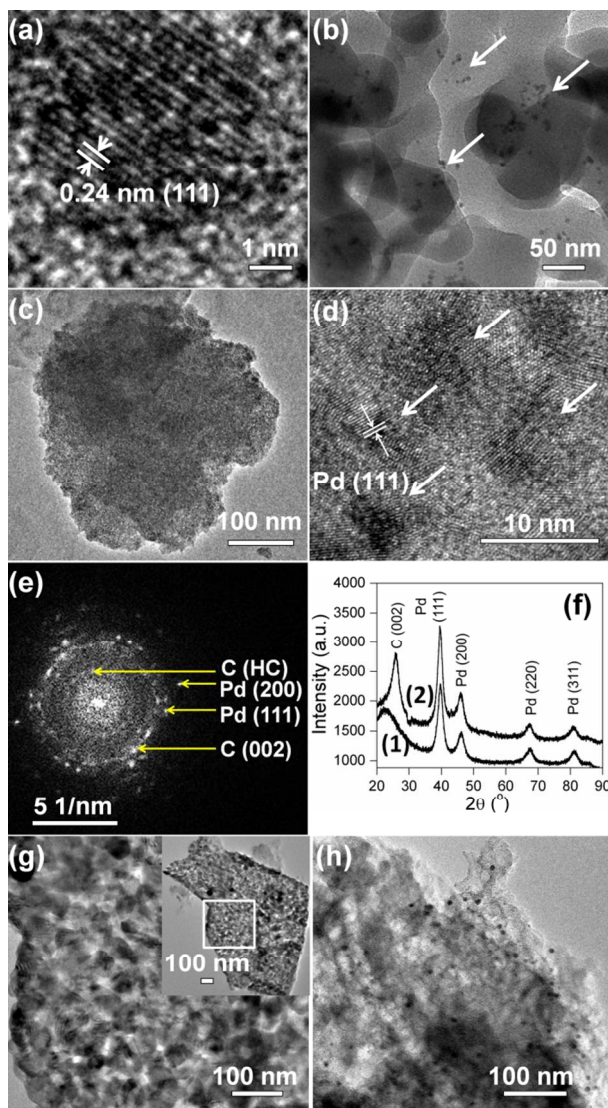


**Figure 3:** TEM images of (a) Pd NP, (b) Pd@SiO<sub>2</sub>, (c, d) Pd@C1. (e) SAED pattern of Pd@C1. HC denotes “high curvature”. (f) XRD patterns of (1) Pd@SiO<sub>2</sub> and (2) Pd@C1. TEM images of (g) Pd@C2, inset shows the entire matrix, and (h) Pd/C.

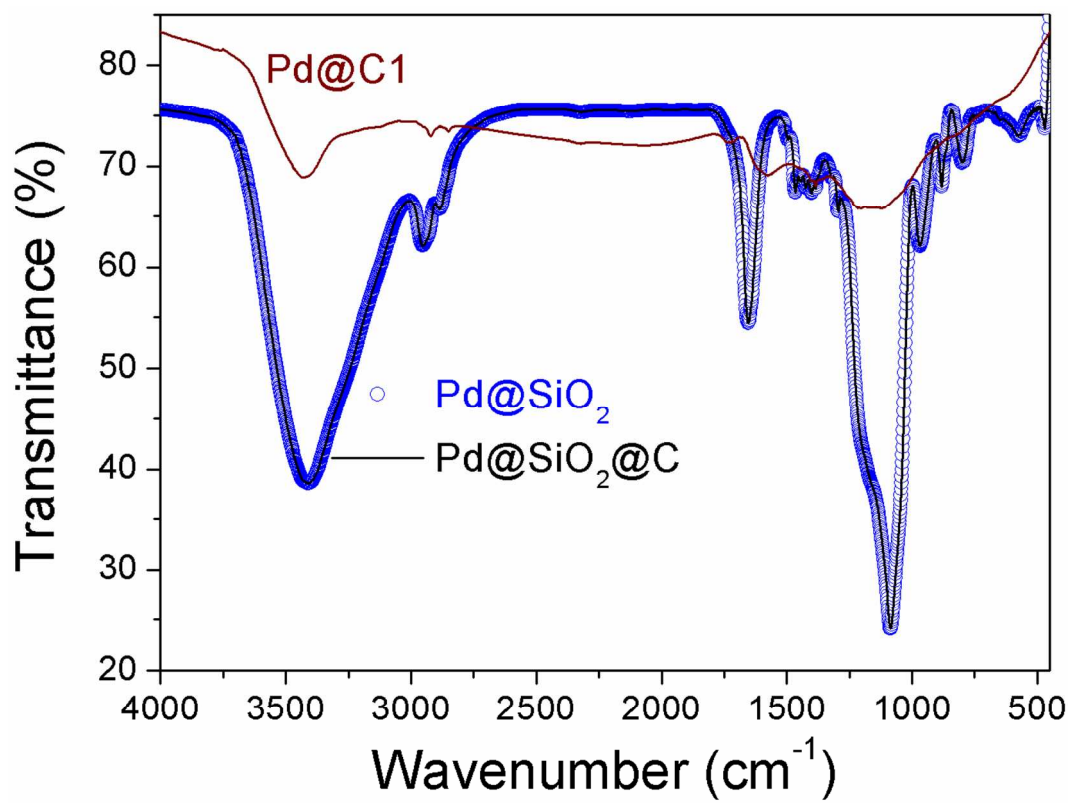


**Figure 4:** FTIR spectra of Pd@SiO<sub>2</sub>, Pd@SiO<sub>2</sub>@C and Pd@C1.

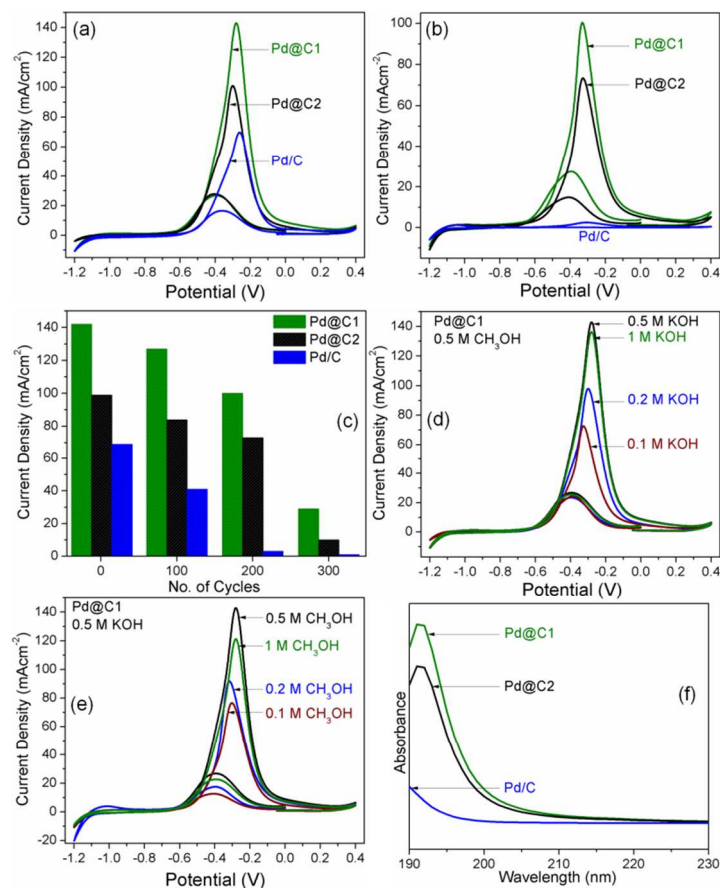


**Figure 5:** CVs for MeOH EOx with the catalyst systems after (a) 1<sup>st</sup> and (b) 200<sup>th</sup> cycle with 0.5 M MeOH and 0.5 M KOH. (c) Bar diagrams showing the changes in AP-CD of the samples up to the 300<sup>th</sup> cycle of electro-oxidation. Performance of Pd@C1 with (d) 0.1 M MeOH and varying concentrations of KOH and (e) 0.1 M KOH and varying concentrations of MeOH. All the plots were obtained after stirring the solutions. (f) Solid state UV-vis absorption spectra of MeOH in the recovered catalysts after 200<sup>th</sup> cycle.

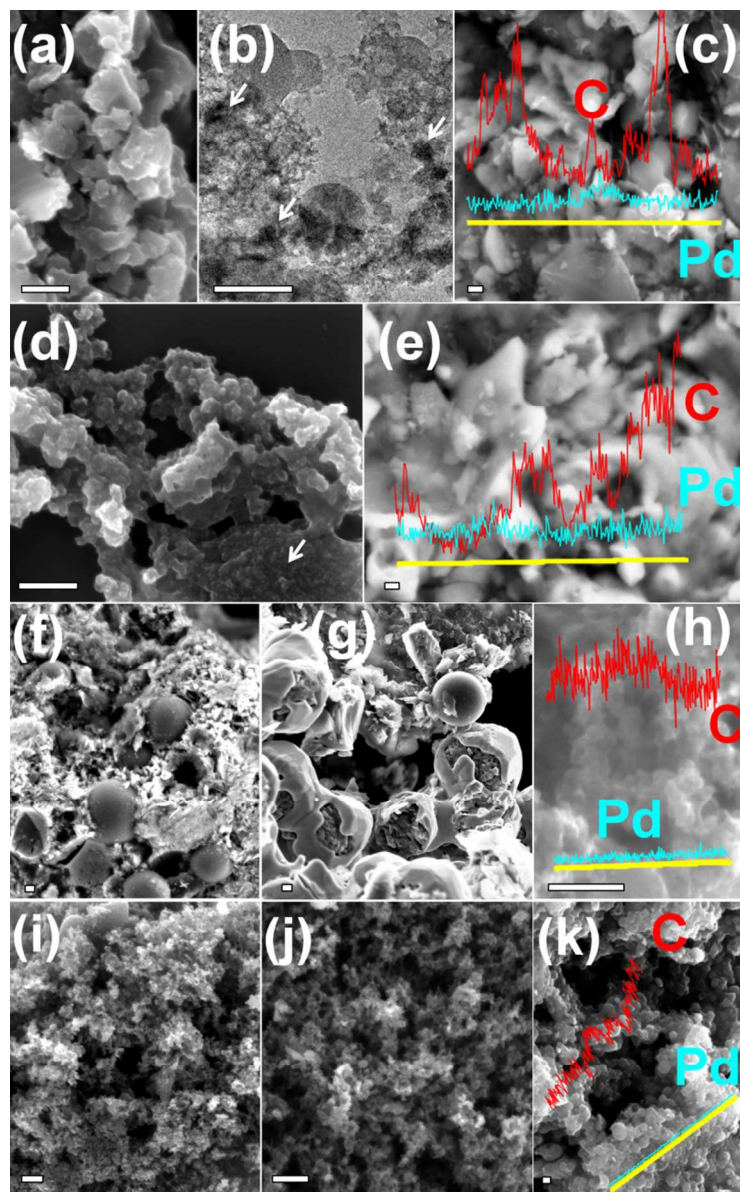


**Figure 6:** (a) FESEM image, (b) TEM and (c) elemental line scan of Pd@C1 after 200 cycles of MeOH EOx. (d) FESEM image and (e) elemental line scan of Pd@C1 after 300 cycles. FESEM images of Pd@C2 after (f) 200 and (g) 300 cycles. (h) Elemental line scan of Pd@C2 after 300 cycles. FESEM images of Pd/C after (i) 200 and (j) 300 cycles. (k) Elemental line scan of Pd/C after 300 cycles. Arrows indicate the agglomerated Pd NPs. All scale bars correspond to 200 nm.

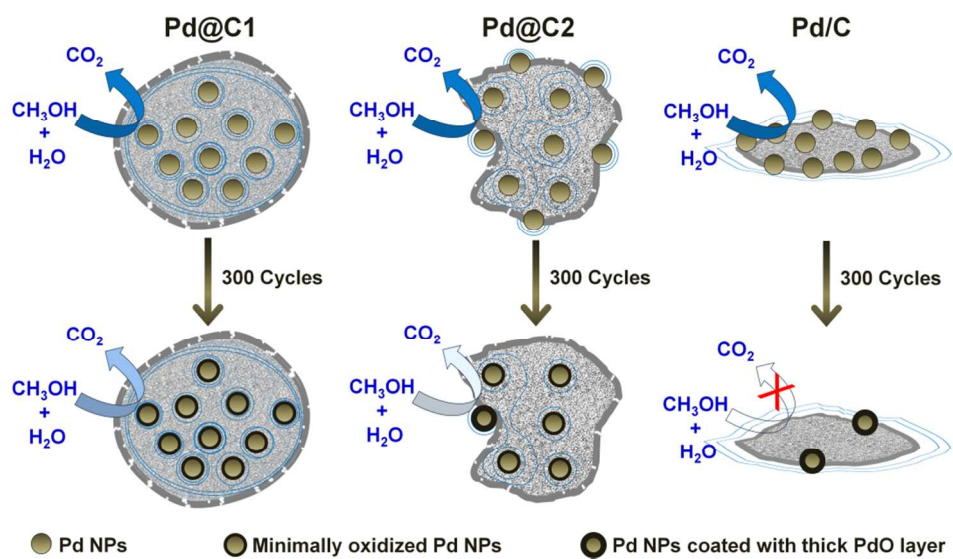


**Figure 7:** Schematic cartoon showing the performance of the catalysts during MeOH EOx in their 1<sup>st</sup> (top panel) and 300<sup>th</sup> (bottom panel). The greater color intensity of the curved arrows indicates better catalytic activity and vice versa.

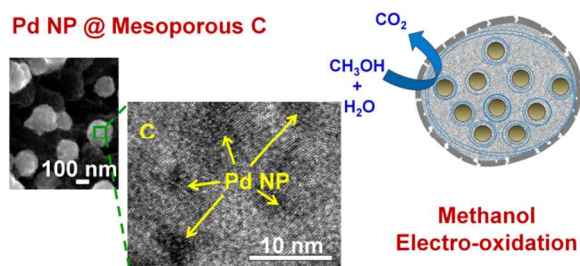
## Enhanced Catalytic Activity of Palladium Nanoparticles Confined inside Porous Carbon in Methanol Electro-Oxidation

Abheek Datta, Sutanu Kapri and Sayan Bhattacharyya\*

*Department of Chemical Sciences, Indian Institute of Science Education and Research (IISER) Kolkata, Mohanpur - 741246, India*

\* Email for correspondence: [sayanb@iiserkol.ac.in](mailto:sayanb@iiserkol.ac.in)

### Table of Contents



Confinement of Pd nanoparticles inside porous carbon leads to enhanced redox properties and high reusability in methanol electro-oxidation reaction.